

Noisy Quantum Simulation Using Tracking, Uncomputation and Sampling

Siddharth Dangwal*, Tina Oberoi*, Ajay Sailopal*, Dhirpal Shah, Frederic T. Chong
University of Chicago

Abstract—Quantum computers have grown rapidly in size and qubit quality in recent years, enabling the execution of complex quantum circuits. However, for most researchers, access to compute time on quantum hardware is limited. This necessitates the need to build simulators that mimic the execution of quantum circuits on noisy quantum hardware accurately and scalably.

In this work, we propose *TUSQ* - Tracking, Uncomputation, and Sampling for Noisy Quantum Simulation. TUSQ is a simulator that can perform noisy simulation of up to 30-qubit Adder circuits on a single Nvidia A100 GPU in less than 820 seconds. To represent the stochastic noisy channels accurately, we average the output of multiple quantum circuits with fixed noisy gates sampled from the channels. However, this leads to a substantial increase in circuit overhead, which slows down the simulation. To eliminate this overhead, TUSQ uses two modules: the *Error Characterization Module* (ECM), and the *Tree-based Execution Module* (TEM).

The ECM tracks the number of unique circuit executions needed to accurately represent the noise. That is, if initially we needed n_1 circuit executions, ECM reduces that number to n_2 by eliminating redundancies so that $n_2 < n_1$. This is followed by the TEM, which reuses computation across these n_2 circuits. This computational reuse is facilitated by representing all n_2 circuits as a tree. We sample the significant leaf nodes of this tree and prune the remaining ones. We traverse this tree using depth-first search. We use uncomputation to perform rollback-recovery at several stages which reduces simulation time. We evaluate TUSQ for a total of 186 benchmarks and report an average speedup of $52.5\times$ and $12.53\times$ over Qiskit and CUDA-Q, which goes up to $7878.03\times$ and $439.38\times$ respectively. For larger benchmarks (more than 15 qubits), the average speedup is $55.42\times$ and $23.03\times$ over Qiskit and CUDA-Q respectively

I. INTRODUCTION

Quantum computing has the potential to offer speedups in tasks like factoring [37], unordered search [17], and physics and chemistry simulations [23], [34]. However, compute time on these devices is still scarce and expensive. It is often available only over the cloud via vendors like IBM [2], Quantinuum [4], and Quera [5] where long queue times are encountered [36]. In order to speed up quantum computing research, we need simulators that accurately mimic the execution of programs on real, noisy quantum hardware. We place a special emphasis on noisy simulations. Most current quantum simulators focus on noiseless simulation, which is not representative of real hardware performance. Hence, simulators that can scalably perform noisy simulation are desirable.

Quantum computing can have a variety of flavors which includes gate-based quantum computing, measurement-based

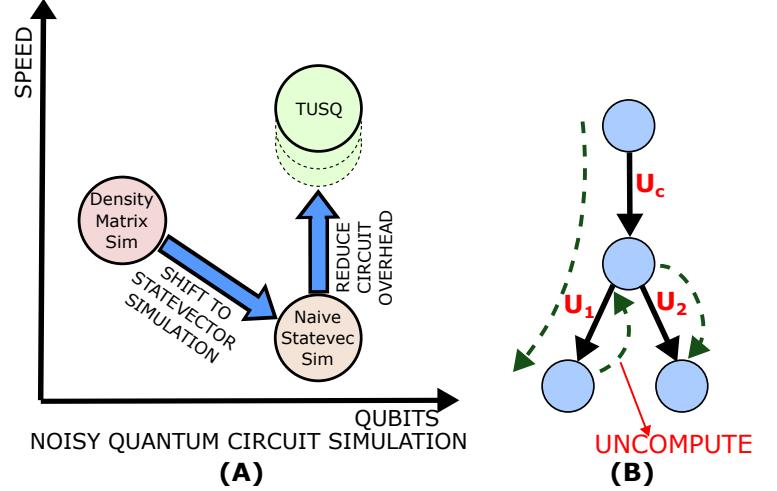


Fig. 1. (A) Using Density Matrix Simulation (DMS) for noisy quantum circuits incurs a high memory overhead. Statevector Simulation consumes lesser memory but is slower because of high circuit overheads. TUSQ achieves fast noisy quantum circuit simulation at a low memory overhead. (B) For circuits with high overlap, TUSQ obtains the final state-vector of the first, uncomputes to an intermediate stage and then carries out the remaining computation for the other thereby saving on computation cost.

quantum computing, and evolution under a continuous-time Hamiltonian [32]. Each of these paradigms needs a different simulation strategy. For this paper, we will simulate gate-based quantum computing which involves starting in a known quantum state, applying discrete operations on it (called gates) to obtain a final quantum state, and finally sampling this quantum state for a finite number of shots to output a classical probability distribution. A larger number of shots better represents the final quantum state, due to reduced sampling error. We call this process *Quantum Circuit Simulation* (QCS).

QCS can be performed with or without noise. In noiseless QCS, we start with a complex vector representing the quantum state and multiply it by deterministic unitary matrices (representing quantum gates) to obtain a final vector. This vector is sampled multiple times to obtain an output distribution. This type of simulation is called *State Vector Simulation* (SVS). Note that the matrix-vector multiplications needed to obtain the final vector need to be performed only once here.

Noisy QCS, on the other hand, encounters stochastic noisy operations which may “manifest” as different gates during different runs. Figure 3 (B) gives an example of one such operation (DEP), which can manifest itself as four different

*These authors contributed equally to this work.

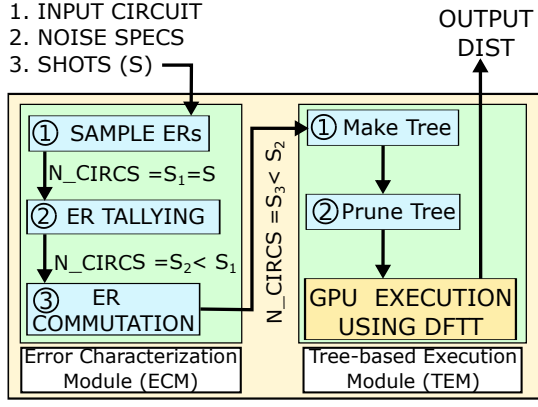


Fig. 2. TUSQ Overview: (A) Error Characterization Module (ECM) - The ECM reduces the number of circuits to be executed from S_1 to S_3 ($S_3 < S_1$). This reduction is achieved by ER tallying and ER commutation. (B) Tree-based Execution Module (TEM): Once we cannot reduce the number of circuits any more, we reuse computation across circuits reducing simulation time even further.

operations ($I/X/Y/Z$) with varying probabilities. To accurately account for the effect of the stochastic noisy operation, we need to perform the entire sequence of matrix-vector multiplications afresh every time we sample the output vector once. Hence, if our output distribution consists of S samples, we need to perform S distinct SVSs resulting in a S -fold time overhead.

An alternative approach is *Density Matrix Simulation* (DMS) which can account for the effect of stochastic noisy operations on a quantum state in one circuit execution. For this, DMS represents quantum states as matrices. Application of quantum operations is represented as matrix-matrix multiplication. Although DMS requires just one circuit execution, the single execution has a quadratically higher memory overhead ($\mathcal{O}(2^{2n})$ as opposed to $\mathcal{O}(2^n)$), which makes it an infeasible choice [7], [22], [33].

This work addresses both speed and circuit size limitations by proposing *TUSQ*: Tracking, Uncomputation, and Sampling for Noisy Quantum Simulation. Similar to CUDA-Q [6], [33] or Qiskit Statevector Simulator [3], TUSQ performs multiple SVSs to represent noisy simulation of one circuit, thereby achieving a quadratically smaller memory footprint than DMS. In order to reduce the resulting time overhead, we propose two modules - *Error Characterization Module* (ECM), and *Tree-based Execution Module* (TEM). The basic principal behind these modules is to identify instances of redundant or relatively unimportant computation and eliminate them which results in fast noisy QCS. Figure 1 (A) shows how TUSQ compares to DMS, and naive SVS in terms of speed and number of qubits.

Performing a series of matrix-vector multiplications to obtain the final state vector of a circuit is much more expensive than sampling the state vector multiple times [33]. Hence, we track all circuit instances where the final state vector would be the same. If there are K such instances, we perform the state vector computation just once and sample it K times instead of performing SVS K separate times. Thus, if initially we needed

n_1 SVSs, ECM reduces that number to n_2 so that $n_2 < n_1$. This is done using ECM. To carry out the tracking process, we use a lightweight intermediate representation of each circuit, which lets us predict whether its output state vector would be unique or not without actually computing it.

Once we are sure that all state vectors would be distinct, the TEM identifies opportunities to eliminate redundant computation across circuits. For example, if two circuits are the same for the first half and differ in the second half, we do not need to perform matrix-vector multiplications from scratch for both. If we assume that all operations on these circuits are unitary, then these circuits are represented as $U_1 U_c$ and $U_2 U_c$ respectively. U_c is the common first half, while U_1 and U_2 are the different second halves of the circuits. We can compute the “final state vector” for the first circuit (say v_1), apply U_1^{-1} to uncompute back to the intermediate state vector and then apply U_2 on this intermediate state vector to get the “final state vector” for the second circuit (v_2) (see Fig 1(B) for reference). This is similar to rollback-recovery performed routinely in classical computer architecture, especially in distributed systems [24]. When generalized for all gates across all circuits, we effectively perform a depth-first tree traversal. We can also prune the tree to eliminate unimportant computation while sampling from only the significantly weighted leaf nodes, further reducing execution overhead. An important assumption here is that all gates in our circuit (even noisy gates) are unitary. As we shall see in Section II-B, this assumption holds for a wide variety of noise models which are reflective of noise on real quantum hardware. Recent work by Wang et. al. [42] also uses a tree data structure to speed up simulation of noisy quantum circuits. However, their design performs memoization of intermediate state vectors similar to [28] as opposed to uncomputation in our case. A detailed analysis of design differences and performance comparison is given in Section VI-B.

The net result of these optimizations is that we can simulate a 30 qubit Adder circuit on a single Nvidia A100 GPU in 819.87 seconds. The same benchmark on popular simulators like CUDA-Q and Qiskit takes more than 10 hours (keeping hardware specifications same). Thus, TUSQ achieves high speed with low memory overhead as shown in Figure 1. Overall, we summarize the key contributions of our work as follows:

- 1) To reduce the high circuit overhead associated with noisy SVS, we propose the *Error Characterization Module* (ECM), that ensures that we only execute circuits with distinct output state vectors.
- 2) To further reduce the cost associated with computing each of those unique output state vectors we propose *Tree-based Execution Module* (TEM), which reuses computation across circuits and gets rid of relatively unimportant computation. Together, the ECM and TEM comprise TUSQ.
- 3) We implement TUSQ in a highly optimized, GPU compatible fashion. An open-source implementation of the code would be provided with the camera-ready version.

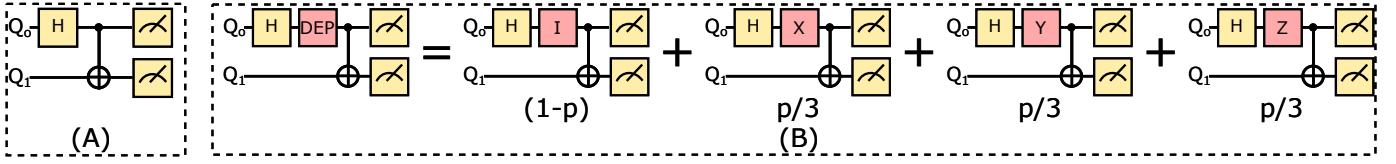


Fig. 3. (A) A noiseless quantum circuit composed of one single- and one two-qubit gate. (B) A noisy version of the quantum circuit (A) with a non-unitary, stochastic depolarizing channel (LHS). This circuit can effectively be seen as a weighted “classical average” of four quantum quantum circuits (RHS) with the weights mentioned. Here ‘p’ is a real parameter between 0 and 1.

- 4) We evaluate TUSQ for a total of 186 benchmarks and report an average speedup of $52.5\times$ and $12.53\times$ over Qiskit and CUDA-Q, which goes up to $7878.03\times$ and $439.38\times$ respectively. For larger benchmarks (more than 15 qubits), the average speedup is $55.42\times$ and $23.03\times$ over Qiskit and CUDA-Q respectively.

II. BACKGROUND

A. Noisy Quantum Circuit Simulation

Quantum programs are represented as a circuit comprising quantum bits (qubits), which are acted upon by operations called quantum gates. This is followed by a measurement operation, which converts quantum information in qubits to a classical bit-string. Typically, a qubit-vector (also called a state vector) is represented as $|\psi\rangle$, and a gate as U . Ideally, in the absence of noise, an n -qubit register can be adequately represented using a 2^n dimensional complex vector such that its l_2 norm is one. A gate acting on k qubits is represented using a $2^k \times 2^k$ dimensional unitary matrix that acts on $|\psi\rangle$ to produce the output vector $|\psi'\rangle$ as shown in equation 1.

$$|\psi'\rangle = U |\psi\rangle = \begin{pmatrix} a_{00} & a_{01} & \cdots & a_{0,2^k-1} \\ a_{10} & a_{11} & \cdots & a_{1,2^k-1} \\ \vdots & \vdots & \ddots & \vdots \\ a_{2^k-1,0} & a_{2^k-1,1} & \cdots & a_{2^k-1,2^k-1} \end{pmatrix} \begin{pmatrix} v_0 \\ v_1 \\ \vdots \\ v_{2^n-1} \end{pmatrix} \quad (1)$$

In the general case $k \neq n$. In this case, U modifies only those amplitudes in $|\psi\rangle$ that correspond to the qubits on which it acts. Figure 3(A) shows a noiseless quantum circuit. The vector representation of a quantum state and the unitary matrix representation of a gate are all part of the *State Vector Formalism*. As mentioned in Section I, a simulation performed in the state vector formalism is called a state vector simulation (SVS).

The statevector formalism works really well when representing noiseless quantum circuits. However, realistic quantum circuits are affected by noise from the environment. In this case, the state-vector formalism is not adequate. We rely on a different formalism called the *Density Matrix Formalism* where qubits are represented as a positive semi-definite Hermitian matrix ρ with trace equal to one [32]. This is called the density-matrix of the qubit. Operations acting on the qubits are represented as a quantum channel which map the matrix ρ to a new matrix ρ' following the equation $\rho' = \sum_i K_i \rho K_i^\dagger$. The matrices K_i are called *Kraus Operators*. All quantum operations, be it noiseless gates or stochastic

noisy channels can be represented using Kraus operators. For example, the application of a noiseless gate U , as given in Equation (1), becomes $\rho' = U\rho U^\dagger$ in the density matrix formalism. Similarly, a depolarizing error channel acts as $\rho' = (1-p)\rho + \frac{p}{3}X\rho X + \frac{p}{3}Y\rho Y + \frac{p}{3}Z\rho Z$. Here, the parameter “p” dictates the intensity of noise. Performing QCS by implementing the equations of the density matrix formalism is called density matrix simulation (DMS). Density Matrix Simulation gives us a very elegant and succinct way to perform noisy QCS. However, as mentioned in Section I, the memory overhead of DMS grows quadratically faster compared to SVS which drastically limits the number of qubits that can be simulated even on large supercomputing clusters [42]. However, there is a way in which SVS can be tweaked to perform noisy QCS with extra overhead. Note that the depolarizing channel output is a sum of multiple terms as opposed to a single term in the case of operation U . Since U is a noise-free operation, each input produces a single deterministic output. In case of an error channel, the output is stochastic and hence represented as a weighted average of all possible outcomes. In case of the depolarizing error channel, the four possible outcomes are that the (a) quantum state stays unchanged, (b) a X gate acts on it, (c) a Y gate acts on it, and (d) a Z gate acts on it. In the density matrix formalism, the output is a weighted sum of these individual possibilities. This output can also be interpreted as a weighted classical mixture of the input state ρ acted upon by unitary gates I, X, Y and Z . This reinterpretation lets us represent the output of noisy QCS as a sum of the outputs of multiple SVSs, each with a “fixed” manifestation of the noisy channels (in our case, the depolarizing channel is substituted by one of its constituent noisy gates - $I/X/Y/Z$).

Thus, to replicate the information conveyed in the density matrix formalism, we have to run multiple instances of the circuit in the state vector formalism and perform a weighted average of the output. This gives us a way to use the state vector formalism even in the presence of noise at the cost of extra circuit overhead as shown in figure 3(B). Tools such as CUDA-Q [6], [33], and Qiskit state vector simulator [3] implement noisy simulation in this way. Note that performing noisy QCS in the state vector formalism introduces statistical errors in our estimate of the noisy output. This error scales as $\frac{1}{\sqrt{S}}$, for S trials of the state vector simulation [41]. In the limit $S \rightarrow \infty$, the results from the SVS and DMS approaches converge. [9], [31], [35], [41].

B. Characterizing Noise

In section I, while introducing the Tree-based Execution Module (TEM), we assumed that all gates in our circuits are unitary. This assumption holds trivially for a variety of noises. For example, measurement noise is modeled as stochastic injection of the X gate while depolarizing noise is modeled as random insertions of $X/Y/Z$ gates. Since all Pauli gates are unitary, our assumption is valid if we account for only measurement and depolarizing noise. Many simulation and theoretical studies, especially those that assume the availability of error correction, account for only these Pauli channels [10], [12], [14], [18], [29], [43]. To account for the impact of decoherence, we use the Pauli-twirling approximations given in [13]. Thus, the effect of decoherence can be expressed as:

$$\rho \rightarrow (1 - p_X - p_Y - p_Z)\rho + p_X X\rho X + p_Y Y\rho Y + p_Z Z\rho Z \quad (2)$$

Here $p_X = p_Y = \frac{1 - e^{-t/T_1}}{4}$, and $p_Z = \frac{1 - e^{-t/T_2}}{2} - \frac{1 - e^{-t/T_1}}{4}$.

Hence, decoherence can also be expressed as stochastic insertions of $X/Y/Z$ gates. This makes our design compatible with a large variety of noise models and covers all practically significant noise sources in quantum hardware [44].

III. MOTIVATION AND PROPOSAL

In Section II we mentioned that using DMS for noisy QCS is not preferred due to its high space overhead. However, when using SVS, we need to simulate many circuits to perform one noisy QCS. In effect, we trade off the space overhead for a higher time overhead in the form of additional circuits. Our primary objective is to reduce the circuit overhead, which effectively reduces the simulation runtime. To achieve our objective, we introduce two modules - the *Error Characterization Module* (ECM), and the *Tree-based Execution Module* (TEM). The ECM is further composed of two steps - (a) ER tallying and (b) ER commutation while the TEM is also composed of two steps - (a) depth-first tree traversal and (b) pruning. The overall schematic of TUSQ is shown in Figure 2

A. Error Characterization Module (ECM)

When using SVS for performing noisy QCS, we naively need to simulate “ S ” circuits instead of one (where S is the number of shots in our output distribution). The goal of ECM is to analyze these S circuits to find instances that produce the same output. In this way, we can reduce computational overhead by sampling multiple times from the same output distribution instead of calculating the distribution afresh every time. To identify these instances we propose two procedures - (a) Error Realization (ER) tallying, and (b) ER commutation.

1) **Error Realization (ER) Tallying:** As shown in Figure 3(B), a circuit with stochastic noisy channels can be seen as a classical average of many circuits with “fixed noisy gates” (the $I/X/Y/Z$ gates remain fixed). We can obtain these circuits with fixed noisy gates from stochastic noisy channel circuits by

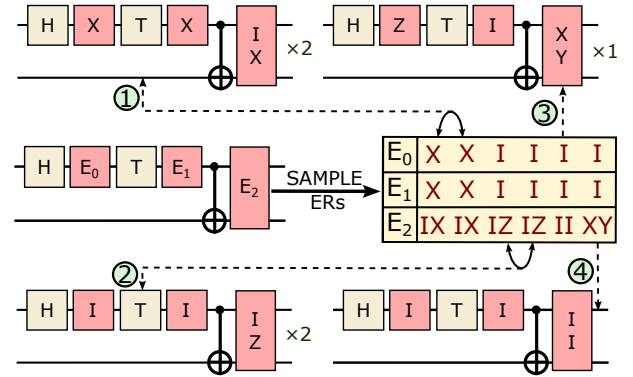


Fig. 4. ER tallying Overview: All the stochastic noise channels in the circuit are sampled to obtain the exact error-realization (ER) for each channel and the combined ER of the circuit. If the ER e_i occurs s_i times, then the corresponding circuit c_i , is simulated once, and its output vector is sampled s_i times. This is in contrast to the naive approach (taken by simulators like Qiskit Statevector Simulator), where the simulation is performed s_i times and the output vector sampled once per simulation.

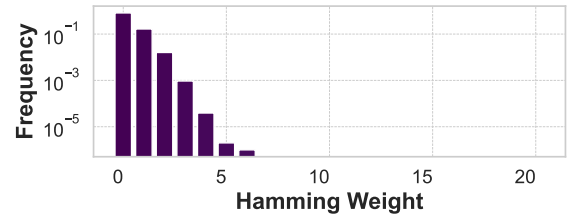


Fig. 5. Frequency of sampled ERs by hamming weight. ERs with lower hamming weight (more I gates) are more frequent

sampling the channels. We call the set of gates sampled from the noise channels per SVS instance an *error realization* (ER). For example, for a depolarizing noise channel with a 10% error rate ($p = 0.1$), the ER could be I (No error) with 90% probability ($1 - p$), and X , Y , or Z (Error) with probability $\frac{10}{3}\%$ each ($\frac{p}{3}$). For a circuit with N different depolarizing channels, the ER would just be the N -tuple of the ERs of each channel. An example ER could be $(I_0, X_1, Y_2, \dots, I_{N-1})$. Currently, on most reasonable quantum computers, the error rate per operation varies between 0.1% and 10%. This results in ERs with low Hamming weights [1], i.e., where most gates correspond to the no-error case - the I gate. Since the probability of the I gate is much higher than the probability of $X/Y/Z$ gates, the lower the Hamming weight of an ER, the higher its probability of occurrence. Figure 5 shows the frequency of ERs as a function of their hamming weights. We observe that the probability of an ER having Hamming weight greater than 6 is zero.

Using this insight, we start to track the frequencies of different ERs. The basic idea is to sample from all error channels and keep a count of the ERs before performing the SVS. If any ER (say e_i) occurs s_i times, we can simulate the corresponding circuit (c_i) once and sample the output state vector s_i times rather than performing s_i separate SVSs. Since sampling an output state vector multiple times is much

cheaper than implementing matrix-vector multiplications [33], ER tallying helps us to reduce the overhead quite substantially. Similar optimization is also performed in [33] to reduce noisy simulation overhead. The high-level overview of ER tallying is shown in Figure 4.

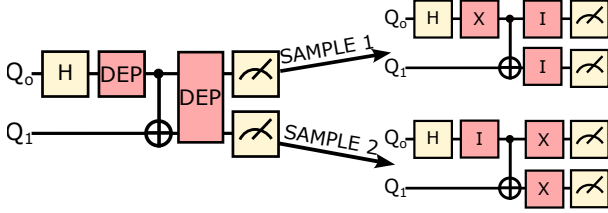


Fig. 6. ER Commutation Overview: The ERs corresponding to the two samples look different - (X, II) vs (I, XX). However, they produce the same output statevector and are equivalent.

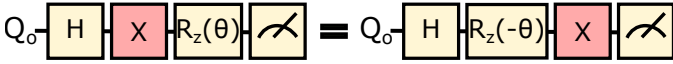


Fig. 7. The circuits on the left and right are equivalent. However, we do not push the noisy X gate through the R_z gate since it changes the argument from θ to $-\theta$ effectively changing the noiseless circuit

2) **ER Commutation:** ER tallying keeps count of the unique ERs and their frequencies. However, there are instances where, despite being different, the ERs produce the same output state vector. Consider the circuit shown in figure 6, and two sample ERs - (X, II) and (I, XX). Since these ERs are different, in general we would naively compute the state vector for each of them separately. However, an X gate on the control qubit of a CNOT operation, when commuted through the CNOT, leads to an extra X gate on the target qubit as well. This can be verified easily by performing the corresponding matrix multiplications. Thus, despite being different, these ERs produce the same result. At a circuit level, this behavior is observed a lot more frequently, which gives us greater opportunity of overhead reduction. ER commutation identifies all such ER instances and groups them together further reducing the number of unique circuits we need to simulate. Mathematically, if (c_1, s_1) and (c_2, s_2) are two (circuit, shot) tuples corresponding to distinct ERs e_1 and e_2 , which produce the same output state vector, then we remove the (c_2, s_2) tuple and update s_1 as $s_1 \rightarrow s_1 + s_2$.

To ensure that c_1 and c_2 produce the same output state vector, we push the noisy gates as far to the right as possible in both circuits. A noisy gate is pushed until it encounters a situation where pushing it further to the right will modify the noiseless circuit. For example, in Figure 6, we push the noisy X gate through the CNOT since none of the noiseless circuit gates (Hadamard, CNOT, and measurement) is altered in this process. However, in Figure 7, we don't push the X gate through the R_z since doing so would alter the argument of R_z from θ to $-\theta$, modifying the noiseless circuit. Once this has been done, we simply compare the new ERs of c_1 and c_2 . If they are the same, we add their counts.

3) **ER Commutation - Algorithm and Implementation:** In order to benefit from ER commutation, we must ensure that the time taken to push the gates is small. If each circuit consists of a total of g_1 gates out of which g_2 are noisy gates, then in the naive case we would need to perform $\mathcal{O}(g_1 \cdot g_2)$ operations per circuit to carry out ER commutation. The process would be similar to bubble sort. If the total number of unique circuits at the end of ER tallying is S_2 , the total number of operations becomes $\mathcal{O}(S_2 \cdot g_1 \cdot g_2)$. This is a high cost.

We can reduce this cost using a greedy algorithm that is very close to optimal in practice. The algorithm starts by initializing a vector of stacks, one stack corresponding to each qubit. Our circuits are assumed to be transpiled into a basis of single-qubit gates and the CNOT gate. The noise sources are measurement noise, depolarizing noise, and the Pauli twirled equivalent of decoherence noise, as mentioned in Section II-B, all of which result in Pauli noisy gates. At every step of the algorithm, we maintain the invariant that noisy gates are pushed as much to the right of the circuit as possible. This invariant is preserved using a set of commutation rules listed below:

- 1) Multiple noisy Pauli gates back-to-back are multiplied together to condense them into a single noisy Pauli gate.
- 2) A noisy Pauli gate can commute through any other noiseless Pauli gate.
- 3) Pauli gates - X/Y/Z commute through rotation gates along the respective axis, i.e. $R_X/R_Y/R_Z$.
- 4) An X gate on the control qubit of a CNOT, when pushed through the CNOT, results in an X gate on both the control and target qubits (see Figure 6). An X gate on the target qubit of a CNOT, when pushed through, results in an X gate only on the target qubit.
- 5) A Z gate on the target qubit of a CNOT, when pushed through the CNOT, results in a Z gate on both the control and target qubits, while a Z gate on the control qubit of a CNOT, when pushed through, results in a Z gate on only the control qubit.
- 6) A Y gate on the control qubit of a CNOT, when pushed through the CNOT, results in a Y gate on the control qubit and an X gate on the target qubit, while a Y gate on the target qubit of a CNOT, when pushed through, results in a Z gate on the control qubit and a Y gate on the target qubit.

We iterate through the gates of our circuit. For each noiseless candidate gate in our circuit, we check the tops of the stacks of the qubits on which the gate acts. If the stack is empty or the top gate is one that doesn't commute with our candidate gate (as per our commutation rules), we push the candidate gate and proceed. If the top of the stack has a noisy gate that commutes (as per the commutation rules 2-6 enumerated below) with the candidate gate, then pop from the stack, push the candidate gate on the stack, and finally push new noisy gates according to the respective commutation rule. For each noisy candidate gate in the circuit, we check the tops of the stacks again. If we find existing noisy gates in the stacks, we simply merge the candidate gate with the existing noisy gates

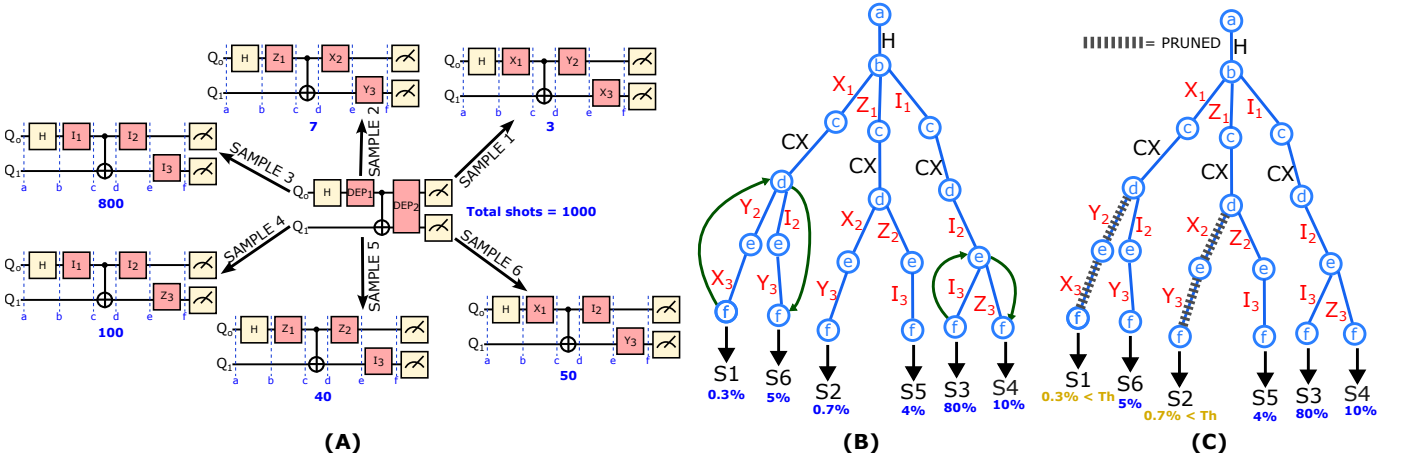


Fig. 8. (A) The figure shows a circuit with two depolarizing channels sampled for a total of 1000 shots. These thousand shots are split amongst 6 distinct circuits. Circuits with more identity gates are more common since realistic error channels have low error probability ($< 10\%$). This means that as the hamming weight of the circuit’s ER increases, the expected number of shots for that circuit decrease. (B) These six output circuits can be represented using a tree. The nodes represent the value of the state vector at a particular point in the circuit. The edges represent gates. For each individual circuit, we can traverse from the root \textcircled{a} to the leaf \textcircled{f} , updating the state vector by multiplying it with the respective edge’s gate to obtain the final state vector. We can also reuse computation. For example, once we have computed output of Sample 1 (S_1), we simply traverse back the edges to node \textcircled{d} , and then down the branch of S_6 (green arrows). Traversing back on an edge means applying the inverse of the gate on the given edge. For the example shown using the green arrows, we don’t have to perform the multiplications from node \textcircled{a} through node \textcircled{d} for S_6 . This is analogous to rollback-recovery routinely used in classical computer architecture. (C) Leaves which contribute a very small amount (less than a threshold calculated using user-specific hyper-parameters) to the final output distribution are pruned to save computation time.

in the stacks according to rule 1, else we push the candidate gate and proceed. This whole procedure maintains the circuit invariant of having noisy gates as much to the right as possible.

This process is repeated till all gates in the circuit are exhausted. Once that is done, we combine the shots of the circuits with the same ER.

B. Tree-based Execution Module (TEM)

Once we have obtained the set of circuits with distinct outputs, we need to perform SVSs of these circuits to obtain their output state vectors. This is followed by sampling and averaging the state vectors to obtain the final output distribution. The most naive way to achieve this is to perform matrix-vector multiplications for each circuit separately. However, we observe that there are many opportunities for computation reuse across circuits. To exploit this opportunity of computational reuse, we propose two procedures - (a) depth first tree-traversal (DFTT) and (b) pruning

1) **Depth-first Tree Traversal (DFTT)**: Figure 8 (A) shows “fixed gate” noisy circuits sampled from stochastic noise channels along with their frequency of occurrence. In this case, we have six distinct samples. Assuming that the number of distinct circuits cannot be further reduced using the ECM, the most naive way to simulate them would be to perform matrix-vector multiplications from the beginning for each of them. However, we can reuse computation by placing these circuits in a tree-like structure as shown in Figure 8 (B).

The nodes \textcircled{a} - \textcircled{f} denote the state vector at their respective positions in the circuit, while the edges represent gates acting on the state vectors (see Figure 8(A)). Every time we travel to a node from its parent node, we update the state vector by multiplying it by the gate corresponding to the edge

between the nodes. If we travel to a node from its child, we update the state vector by multiplying it by the inverse of the corresponding gate. Note that we have a valid inverse for all our gates, since all gates, noisy or noiseless are unitary, as discussed in Section II-B. The output of a circuit can be computed by traversing the root (\textcircled{a}), all the way to the leaf (\textcircled{f}) for that circuit.

Once we have reached the leaf, we can reuse parts of the computation to reach other leaf nodes. For example, in Figure 8(B), once we have reached the output of S_1 , we can follow the green arrows to obtain the output of S_6 , without having to traverse nodes \textcircled{a} - \textcircled{d} again. In essence, we rollback to a previous state and proceed from there instead of starting from scratch for S_6 which saves us many matrix-vector multiplications. As the circuit gets larger, these benefits multiply. An alternative approach employed by other simulators while reusing computation across circuits is memoization of intermediate state [42], [27]. For example, these simulators would save the state in node \textcircled{d} , when computing S_1 , and start from there when computing S_6 instead of starting from scratch. However, the memory footprint of this method grows very quickly, doubling every time we save an intermediate state. In contrast, we do not save any extra states. Rather, we just roll back to a branching node. An argument in favor of the memoization approach is that it leads to maximum utilization of available memory. In case of DFTT, we make use of additional available space by traversing multiple sub-trees parallelly. Figure 9 (B) illustrates this phenomenon. For example, if we are utilizing only 25% of the total available GPU memory, we can copy the state in the root node down to the respective roots of the four sub-trees and perform DFTT

on them in parallel. Thus we are able to utilize GPU memory effectively while also achieving an orthogonal speedup. Note that the critical factor which enables us to perform the rollback step is the unitary nature of all gates (even the noisy ones which we justify in Section II-B). If the gates are not unitary, we cannot perform reversible computation and the rollback step becomes infeasible.

2) **DFTT-Asymptotic Complexity:** In this section, we formally show the asymptotic advantage obtained by performing DFTT instead of naive simulation.

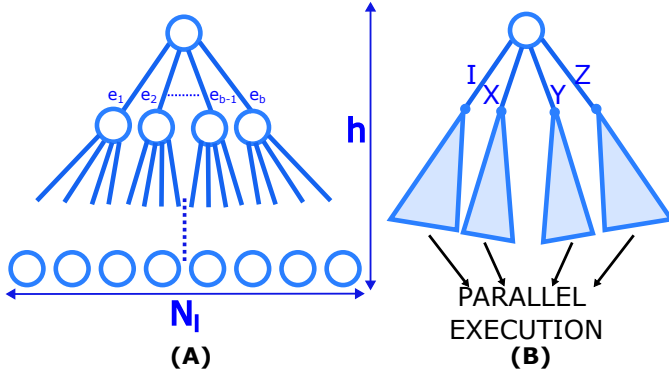


Fig. 9. (A) For a depolarizing noise model, every node has 4 child nodes. In case of measurement noise, there are just 2 child nodes. (B) When we have extra memory available, we can copy a state from a node to a subset of its children and traverse multiple sub-trees in parallel. This leads to optimal use of available memory and gives an orthogonal speedup to the one already present in DFTT

Consider a noise model where after every gate we apply a noisy channel with b different possibilities $\{e_1, e_2, \dots, e_b\}$. For example, in the case of single qubit depolarizing noise $b = 4$ ($\{I, X, Y, Z\}$), and in the case of measurement noise $b = 2$ ($\{I, X\}$) (see Figure 9 (A)). For simplicity, we will assume the value of b to be fixed throughout the circuit. This noise model creates a tree in which the number of nodes at each level grows exponentially. Let the total number of edges in the tree be $|E|$, the height of the tree be h and the number of leaf nodes be N_l (see Figure 9B). For DFTT, the number of operations (T_{dftt}) is equal to the number of edge traversals. We traverse every edge twice, which gives us $T_{dftt} = 2|E| = \mathcal{O}(|E|)$. In the naive implementation, we traverse all the way from the root to a leaf node for every leaf node. The number of such traversals is equal to the number of leaves, which is N_l . The number of edges in each traversal is equal to the height of the tree. Hence $T_{naive} = N_l \times h$. Note that, at every tree level, the number of edges grows exponentially by a factor of b . Hence, $b + b^2 + \dots + b^h = |E| \implies b \cdot \left(\frac{b^h - 1}{b - 1}\right) = |E| \implies h = \log_b((b - 1)|E| + b) - 1$

Also note that the number of leaf nodes is equal to the number of edges at the last level (since each edge connects to one unique leaf node), which gives us $N_l = b^h = (1 - \frac{1}{b})|E| + 1$.

Using these two expressions, we get $T_{naive} = N_l \times h = ((1 - \frac{1}{b})|E| + 1) \times (\log_b((b - 1)|E| + b) - 1) = \mathcal{O}(|E| \log_b |E|)$. Thus, DFTT reduces the number of operations from $\mathcal{O}(|E| \log_b |E|)$ to $\mathcal{O}(|E|)$.

3) **Pruning:** In Figure 8 (A), we see the associated number of shots with each circuit that we sample. Note that circuits with more I gates have a higher frequency of occurrence for reasons that we discuss in Section III-A1. We call these high-frequency circuits the *significant circuits*. The low frequency circuits do not contribute much to the output probability distribution and we call them the *insignificant circuits*. If the frequency of the most commonly occurring circuit is p_0 , then we define a constant α such that any circuit with frequency $p_i \geq \alpha \cdot p_0$ is a significant circuit, else it is insignificant. For this paper, we choose $\alpha = 0.01$, which makes samples 1 and 2 insignificant and the rest significant ($\alpha \cdot p_0 = 0.01 \times 800 = 8$).

Since these circuits are supposed to signify noise, which itself has stochasticity associated with it, eliminating circuit instances with low weights would introduce only a negligibly small perturbation to the circuit. Hence, for the significant circuits, we obtain the output state vector and sample it normally. However, we prune the branches corresponding to the insignificant circuits from our tree as shown in Figure 9 (A).

However, we often encounter cases where the individual frequency of each insignificant circuit is small; however, the sum of their frequencies (say f_{insig}) is substantial. For example, when simulating a 10 qubit QAOA circuit for a million shots, the significant circuits account for 58%, while the insignificant circuits account for 42% of the total shots. In this case, simply ignoring all insignificant circuits introduces a large error. Hence, we randomly sample a subset of insignificant circuits $\mathcal{K} = \{(c_{t_1}, p_{t_1}), (c_{t_2}, p_{t_2}), \dots, (c_{t_\beta}, p_{t_\beta})\}$. The number β is a user-chosen hyperparameter. We compute the final state vector v_{t_i} for each element in \mathcal{K} , and sample it for a total of $\frac{p_{insig}}{\sum_{i=1}^{\beta} p_{t_i}} \cdot p_{t_i}$ times. This ensures that the total contribution of the set of insignificant circuits is maintained in the output distribution, even though each circuit's individual impact to the output is not very noticeable. We provide bounds on the error introduced by Pruning in the following section

4) **Pruning - Bounds:** We start with a pure state $|\psi\rangle$ with an equivalent density matrix $\rho_0 = |\psi\rangle\langle\psi|$. Suppose that after passing through the circuit, the final density matrix is ρ . In order to sample from a density matrix in the computational basis, we need to perform the eigenvalue decomposition of ρ , then pick an eigenvector (with probability denoted by its corresponding eigenvalue), and then sample from that eigenvector in the computational basis. Suppose that the eigenvalue decomposition of ρ is

$$\rho = \sum_i \lambda_i |\psi_i\rangle\langle\psi_i| \quad (3)$$

where $|\psi_i\rangle$ is the i^{th} eigenvector and λ_i is the corresponding eigenvalue.

Alternatively, we can also represent ρ as an ensemble of state vectors, each corresponding to a different sampled ER. Suppose that we have M distinct ERs after the ECM. For each ER e_j , the corresponding state vector at the end of that circuit

is $|\phi_j\rangle$ with the probability of e_j being p_j . Hence ρ can also be written as

$$\rho = \sum_j p_j |\phi_i\rangle \langle \phi_i| \quad (4)$$

Let us now mathematically compute the probability of sampling the state $|k\rangle$ in the computational basis, where $k = 0, 1, 2, \dots, 2^n - 1$ (n is the number of qubits). As mentioned earlier, we have

$$\begin{aligned} P(k) &= \sum_i P(k/|\psi_i\rangle) \cdot p(|\psi_i\rangle) \\ \Rightarrow P(k) &= \sum_i \lambda_i P(k/|\psi_i\rangle) \\ \Rightarrow P(k) &= \sum_i \lambda_i \|\langle k|\psi_i\rangle\|^2 \\ \Rightarrow P(k) &= \sum_i \lambda_i \langle k|\psi_i\rangle \langle \psi_i|k\rangle \\ \Rightarrow P(k) &= \langle k|\sum_i \lambda_i |\psi_i\rangle \langle \psi_i|k\rangle \\ \Rightarrow P(k) &= \langle k|\rho|k\rangle \text{ (From equation 3)} \\ \Rightarrow P(k) &= \langle k|\sum_j p_j |\phi_j\rangle \langle \phi_j|k\rangle \text{ (From equation 4)} \\ \Rightarrow P(k) &= \sum_j p_j \langle k|\phi_j\rangle \langle \phi_j|k\rangle \\ \Rightarrow P(k) &= \sum_j p_j \langle k|\phi_j\rangle \langle \phi_j|k\rangle \\ \Rightarrow P(k) &= \sum_j p_j \|\langle k|\phi_j\rangle\|^2 \\ \Rightarrow P(k) &= \sum_j p_j P(k/|\phi_j\rangle) \end{aligned}$$

Let $p_o = \max_i(p_i)$, be the maximum probability of all p_i s.

$$\Rightarrow P(k) = p_o \sum_j \frac{p_j}{p_o} P(k/|\phi_j\rangle)$$

Note that $P(k/|\phi_j\rangle) \leq 1$. Pruning simply attempts to remove those samples “ j ”, which have a much smaller probability (p_j) compared to the maximum probability value p_o , i.e. if $\frac{p_j}{p_o}$ is small, we discard that sample.

The rationale behind pruning is that since $\frac{p_j}{p_o}$ is small, discarding it would not change the value of $P(k)$ too much. However, since there is also a summation, we cannot discard those terms with impunity. Therefore, pruning replaces terms with a small $\frac{p_j}{p_o}$ value with an “effective subset” of the population, that is, if the set of all j with small $\frac{p_j}{p_o}$ is \mathcal{I} , then we create a set $K \subset I$, such that K represents the “average effect” of all elements of I taken together. To ensure that all probabilities add to 1 after replacing the samples in \mathcal{I} with the elements of the set \mathcal{K} , we scale each of these probabilities by a factor γ (as defined in Section III-B3).

As described in section III-B3, a circuit is “insignificant” (element of \mathcal{I}) if $\frac{p_j}{p_o} < \alpha$. We denote the set of all circuits by \mathcal{C} . Thus, the probability of state k in the computational basis changes from $P(k)$ (original distribution) to $P'(k)$ (distribution post pruning) as follows:

$$\begin{aligned} P(k) &= p_o \sum_{j \in \mathcal{C} \setminus \mathcal{I}} \frac{p_j}{p_o} P(k/|\phi_j\rangle) + p_o \sum_{j \in \mathcal{I}} \frac{p_j}{p_o} P(k/|\phi_j\rangle) \\ P'(k) &= p_o \sum_{j \in \mathcal{C} \setminus \mathcal{I}} \frac{p_j}{p_o} P(k/|\phi_j\rangle) + p_o \gamma \sum_{j \in \mathcal{K}} \frac{p_j}{p_o} P(k/|\phi_j\rangle) \end{aligned}$$

Where $\gamma = \frac{\sum_{j \in \mathcal{I}} p_j}{\sum_{j \in \mathcal{K}} p_j}$

We bound the error between the original and pruned distributions using the triangle inequality

$$\begin{aligned} |P(k) - P'(k)| &= p_o \left| \sum_{j \in \mathcal{I}} \frac{p_j}{p_o} P(k/|\phi_j\rangle) - \gamma \sum_{j \in \mathcal{K}} \frac{p_j}{p_o} P(k/|\phi_j\rangle) \right| \\ &\leq p_o \left| \sum_{j \in \mathcal{I}} \frac{p_j}{p_o} P(k/|\phi_j\rangle) \right| + p_o \gamma \left| \sum_{j \in \mathcal{K}} \frac{p_j}{p_o} P(k/|\phi_j\rangle) \right| \\ &\leq p_o \alpha |\mathcal{I}| + p_o \gamma \alpha |\mathcal{K}| \\ &= p_o \alpha (|\mathcal{I}| + \gamma |\mathcal{K}|) \end{aligned}$$

Note that empirically, the error introduced by pruning is much lower than this upperbound as will be discussed in Section V-B. Finding tighter bounds to get better theoretical guarantees remains part of future work.

IV. METHODOLOGY

A. Evaluation Infrastructure

TUSQ is built on top of Nvidia’s cuQuantum library [6]. All benchmarking experiments were performed on the NERSC *Perlmutter* supercomputer. Each compute node is equipped with an AMD EPYC 7763 CPU (64 cores/128 threads), and NVIDIA A100 (40 GB) GPUs. For all experiments, computations were restricted to a single GPU using the `CUDA_VISIBLE_DEVICES=0` environment variable.

B. Benchmarks

For our evaluation, we use the following benchmarks from the Supermarq [39] benchmark suite.

1) *QAOA*: : QAOA is a widely studied algorithm that is used to find approximate solutions to constraint satisfaction problems [11]. The circuit consists of p layers of a parameterized building block (higher p means greater depth). The building block consists of layers of single-qubit parameterized gates on all qubits, followed by entangling operations in the form of CNOT gates. QAOA is a useful benchmark since it can be scaled both in terms of depth and number of qubits easily, thus providing a way to evaluate the limits of the simulator along both axes. For our evaluations, we vary the number of qubits from 13 to 25 for $p = 2, 4, 6, 8, 10$.

2) *Adder*: : An adder is a commonly used subroutine in many quantum applications [37]. There are different ways to implement a n qubit adder circuit, each requiring a different number of ancillas and gates. We use the Cuccaro adder [8]. For addition of two n -bit numbers, the Cuccaro adder has $2n + \mathcal{O}(1)$ depth, and uses just one ancilla qubit. For our evaluations, we vary the number of qubits from 14 to 28.

3) *Bit Code*: : A bit code circuit is characterized by a parameter called the code-distance (d). A bit code of distance d , has $2d + 1$ data qubits, and $2d$ ancilla qubits, resulting in a total of $n = 4d + 1$ qubits. For our purpose, we initialize the qubits in the $|0\rangle^{\otimes n}$ state. This is followed by application of CNOTs and Hadamards for a total of d rounds. The purpose of the bit code circuit is to make sure that the input state of the quantum state stays preserved throughout the computation and it doesn’t encounter any errors that flip a $|0\rangle$ state to a $|1\rangle$ state. For our evaluations, we vary the total number of qubits from 5 to 25 (Corresponding to code distances ranging from 1 to 6)

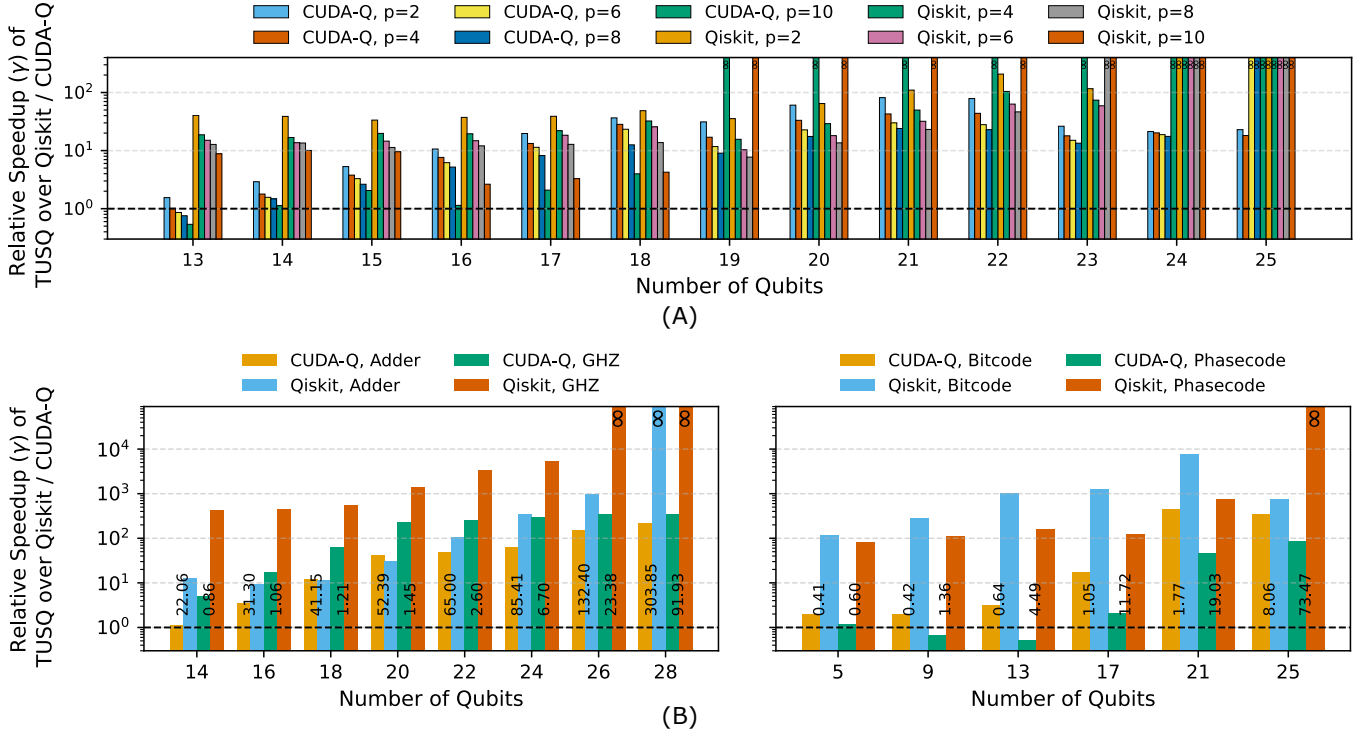


Fig. 10. Relative Speedup Offered by TUSQ over Qiskit and CUDA-Q for QAOA (Subplot A), and Adder, GHZ, Bitcode and Phasecode (Subplot B). In the second sub-plot, the numbers in black over the bars is the time taken by TUSQ (in seconds) to simulate the program. The height of a bar quantifies how much longer it took for CUDA-Q/Qiskit to simulate the same program relative to TUSQ. The higher the bar, the greater TUSQ's speedup. There are cases where the program timed out since the estimated simulation time is more than the Perlmutter limit. These are represented with a bar reaching the roof of the plot and marked with a rotated ∞ sign. TUSQ is the fastest simulator for 181 out of 186 benchmarks. There are five cases where CUDA-Q outperforms TUSQ (9 and 13 qubit Phasecode and 13 qubit QAOA with p=6, 8 and 10). These cases correspond to small programs with fast simulation speed. In this case, the CPU overhead from TUSQ becomes the bottleneck and a naive GPU simulation done by CUDA-Q is faster since CPU overheads are avoided. However, practically the simulation time is low in both cases with TUSQ simulating these programs in 1.36, 4.49, 29.37, 44.20, and 77.14 seconds respectively. Compared to Qiskit, TUSQ's average relative speedup is $52.50\times$, and upto $7878.03\times$. Compared to CUDA-Q, the relative speedup is $12.53\times$ and goes up to $439.38\times$. For larger programs sizes (greater than 15 qubits only) the average relative speedups are $55.42\times$ relative to Qiskit and $23.03\times$ relative to CUDA-Q.

4) *Phase Code*: The phase code circuit is very similar to the Bit code circuit in terms of scaling of qubits and circuit depth with code distance. The type of operations are also just Hadamards and CNOTs, arranged in a slightly different way compared to the Bit Code. The only difference is that the Phase Code preserves the phase information as opposed to amplitude in the Bit Code. The qubits are initialized in the $|+\rangle^{\otimes n}$ state. The objective of the circuit is to prevent individual qubits from changing from the $|+\rangle$ to the $|-\rangle$ state. For our evaluations, we vary the total number of qubits from 5 to 25 (Corresponding to code distances ranging from 1 to 6)

5) *GHZ*: A GHZ state is one of the most fundamental resources in quantum computing. The n qubit GHZ state is $(|\psi_n\rangle = \frac{1}{\sqrt{2}}(|00\dots 0\rangle_n + |11\dots 1\rangle_n))$. The circuit used for the construction of $|\psi_n\rangle$ comprises of n qubits. A Hadamard gate is applied on the 0^{th} qubit, followed by $n - 1$ CNOTs. For the i^{th} CNOT gate, the control qubit is 0 and the target qubit is i . For our evaluations, we vary the number of qubits from 14 to 28.

C. Metrics

1) *Speedup ($\gamma_{A/B}$)*: This metric quantifies the simulation speedup of protocol "A" with respect to protocol "B" as the ratio of the time taken by protocol "B" to that of the time taken by protocol "A".

$$\gamma_{A/B} = \frac{\text{simulation_time}_B}{\text{simulation_time}_A} \quad (5)$$

2) *Relative Fidelity Difference ($\delta_{A,B}$)*: Relative Fidelity Difference quantifies the deviation in fidelity reported by protocols A and B for the same program. If the fidelity of protocol A is f_A , and fidelity of protocol B is f_B , we have

$$\delta_{A,B} = \frac{|f_A - f_B|}{f_A + f_B} \quad (6)$$

where $0 < f_A, f_B \leq 1$ and $0 \leq \delta_{A,B} \leq 1$.

D. Noise Modeling

We currently evaluate TUSQ for depolarizing and measurement noise channels. The probability of error is taken to be $p = 1\%$. As mentioned in Sections I and III-B1, we assume that our noise channels are sampled to produce Pauli errors.

This assumption holds trivially true for both depolarizing and measurement noises and can also be extended to decoherence noise, as mentioned in Section II-B.

E. Baseline

We compare TUSQ against two GPU noisy simulators - Nvidia’s CUDA-Q version 0.11.0 and IBM’s Qiskit version 2.1.0, with Qiskit-Aer version 0.17.0 as the simulation backend. These simulators are popular software tools with extensive documentation which makes it easy to compare TUSQ against them.

V. EVALUATION

A. Speedup

Figure 10 shows the performance of TUSQ compared to Qiskit and CUDA-Q for 186 benchmarks. The height of each bar represents the value of the relative speedup. Some bars touch the roof of the plot and are marked with an ∞ sign. These correspond to cases which could not be completed in 40 hours and timed out on Perlmutter.

TUSQ outperforms Qiskit on all benchmarks, and CUDA-Q on 181 out of 186 benchmarks. The benchmarks where TUSQ is worse than CUDA-Q are the 9 and 13 qubit Phase Code, and the 13 qubit QAOA with $p=6,8$ and 10. These are small programs with fast simulation times where TUSQ’s preprocessing overheads on CPU end up being the bottleneck instead of the GPU compute time. In these cases, a naive GPU simulation with minimal pre-processing, as performed by CUDA-Q turns out to be a better strategy. Practically, the time taken by TUSQ to simulate these programs is also small. TUSQ takes 1.36, 4.49, 29.37, 44.20, and 77.14 seconds to simulate these circuits respectively.

We observe that in general, TUSQ’s relative speedup increases with number of qubits. This is expected since simulation time scales exponentially in the number of qubits. Hence, any improvement in simulation speed would also scale exponentially.

Another trend that we observe in Subplot (A) of Figure 10 is that keeping the number of qubits fixed, the speedup reduces with increase in the value of p i.e. speedup is less for deeper circuits. This happens because of the reduction in the effectiveness of pruning at larger depths. For small values of the error rate, p , the $II...I$ ER with a probability of $(1-p)^g$ is the most frequent one. Here, g is the number of gates, and $p \sim 0.1 - 10\%$. This value decreases rapidly as the circuit depth increases. At the same time, the total number of ERs also increases (while keeping the number of distinct outputs the same) which results in post commutation ERs having higher frequencies. Hence, we end up in a situation where our most frequently-occurring ER’s probability is reduced, while the probability of other ERs increases. This results in an increased number of significant branches and a reduced number of pruned branches in the DFTT tree. This results in an increase in simulation time, and a subsequent reduction in speedup as the depth of the circuit increases.

Although, we have not included an analysis in the current draft, we also anticipate the relative speedup offered by TUSQ to reduce with the increase in p , using the same reasoning. With increasing p , more branches of the tree would be considered “significant” reducing any pruning associated benefits. However, our assumed error rate of 1% is fairly representative of current systems. With improvement in hardware technology, the value of p would only reduce making TUSQ a viable simulation tool even in the future.

Compared to Qiskit, TUSQ’s average relative speedup is $52.50\times$, and upto $7878.03\times$. Compared to CUDA-Q, the relative speedup is $12.53\times$ on average and goes up to $439.38\times$. For larger programs sizes (greater than 15 qubits only) the average relative speedups are $55.42\times$ for Qiskit and $23.03\times$ in case of CUDA-Q.

B. Deviation in Fidelity

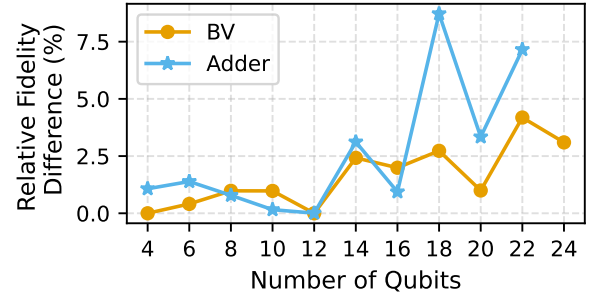


Fig. 11. Relative fidelity difference caused by pruning for BV and Adder. Pruning is the only potential source of fidelity loss in TUSQ. All other steps are perfectly fidelity preserving. We see a relative fidelity difference of 2.1% on average, which goes up to 8.7%.

The pruning step in TUSQ eliminates certain branches of the tree which might lead to deviation in fidelity from the baseline. Note that all other steps of the pipeline - ER Tallying, ER Commutation, and DFTT are fidelity preserving. It is just the pruning step which can lead to potential fidelity loss. Figure 11 shows Relative Fidelity Difference between the pruning, and no-pruning approaches ($\delta_{\text{pruning}, \text{no-pruning}}$) for two benchmarks - BV and Adder. These values have been calculated for $\alpha = 0.01$ and $\beta = 100$. The size of benchmarks varies from 4 to 24 qubits. The average value (arithmetic mean) of δ is 2.1% and the maximum value is 8.7%. Note that geometric mean is not a valid metric in this case, since δ is equal to 0 for a few cases.

Although a strict trend for δ cannot be predicted because of its dependence on many variables, we generally expect its value to increase as the number of gates in the circuit increases. This is because more gates implies a greater number of error channels which makes the ER frequency distribution less skewed. A less-skewed probability distribution deviates more from the original when we chop off its tail.

Another thing to note is that lower δ values can be achieved at the cost of increased simulation time. If the user wants less fidelity deviation, then a lower value of α and a higher value

of β parameters should be used. The exact values to be used is based on user preferences.

VI. DISCUSSION

A. Related Work

An extensive amount of work has been done to improve noiseless circuit simulation speed and reduce memory overheads. Refs [45], [48] use sparsity and data compression to simulate more qubits. FlatDD [21] and BQSim [20] use decision diagrams to represent quantum circuits in a memory efficient way. BQSim uses decision diagrams in the context of batched simulation of a circuit for multiple inputs. Hybrid simulators like HyQuas [46] switch between multiple approaches to quantum circuit simulation based on patterns in the circuit hence leveraging the best method for each part. qHipster [38] implements a distributed quantum circuit simulator. DM-Sim [26] proposes a way to perform efficient density matrix simulations.

There exist simulators which are especially optimized for subclasses of circuits. Stim [14] is extensively used in error correction research to simulate stabilizer circuits in polynomial time. MatchCake [15], [16] is used to simulate matchgate circuits in polynomial time. There are also application specific simulators - Refs [19], [30], [40] perform efficient simulation of variational circuits.

Extensive work has also been done on simulations specifically performed on GPUs. Refs [20], [25], [46], [47] optimize various components of GPU simulation workflow. Note that many of the aforementioned simulators can be easily integrated into TUSQ by replacing the CuQuantum backend with them.

Past work has also looked at noisy circuit simulation. Refs [27], [42] reduce noisy circuit simulation overhead by using memoization of intermediate states. A detailed comparison against Ref [42] - TQSim, has been given in VI-B

B. Comparison Against TQSim

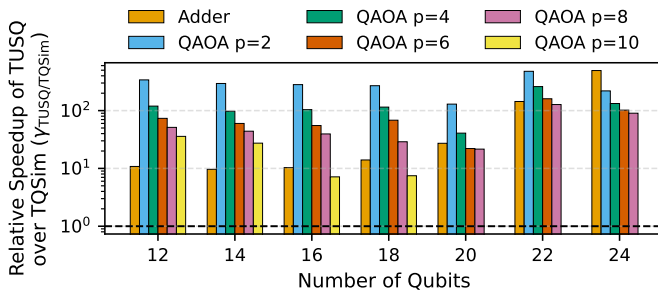


Fig. 12. Speedup offered by TUSQ over TQSim for Adder and QAOA. TUSQ is on average $68.6\times$, and upto $493.4\times$ faster than TQSim.

Recently published work TQSim by Wang et. al. [42] also uses a tree data structure to speed up noisy quantum simulation. Despite peripheral similarities, there are marked differences in the design and performance of the two methods. We discuss the design differences :

- 1) TQSim traverses its tree using breadth-first search, simulating nodes at the same depth together. The states at intermediate nodes are memoized and used later in the computation as we traverse down the tree. This is in contrast to TUSQ, where we traverse the tree in a depth-first fashion. No memoization is needed. We uncompute back to intermediate states as shown in Figures 1 (B) and 8 (B).
- 2) TUSQ uses ERs as an intermediate representation (IR) to determine whether two circuits give the same output or not without actually computing it. This lets us reduce overhead while ensuring minimal Relative Fidelity Deviation (δ). This is done by analysing the ER of each circuit and grouping together circuits only with same ERs and sharing computation across circuits with overlapping ERs only (at all steps except Pruning where we use statistical methods). This is in contrast to TQSim where no IR is used. Rather there is a reliance on statistics to determine how much computation can be eliminated at each step while trying to minimize fidelity loss (δ). Thus, the aggressiveness of all of TQSim's optimizations is controlled by the amount of fidelity approximations they introduce at each step, which is not the case for the first three out of the four optimizations of TUSQ.
- 3) TQSim's speedup is also dependant on the factors like extra available memory and state copy overheads [42]. TUSQ's speedup is algorithmic as shown in Section III-B2. We do not store or copy states means no additional memory is needed. All computation and uncomputation is performed only on a single state-vector stored in the CPU/GPU memory. In case extra memory is available, TUSQ parallelizes the DFTT step introducing an orthogonal speedup to the one already offered by DFTT.

TQSim and TUSQ are orthogonal enough where their designs can be combined together. Currently, the way TUSQ utilizes additional memory is for parallelizing the DFTT step as shown in Figure 9(B). While this is effective, TQSim's design might prove to be a better strategy on efficient use of extra memory. The resulting simulator could perform memoization till memory saturation as dictated by TQSim. This would also eliminate the need to perform computation till a particular tree depth. The resulting sub-trees can simply be traversed using DFTT to obtain the final output distribution.

To evaluate the performance of TUSQ against TQSim, we compute the relative speedup ($\gamma_{TUSQ/TQSim}$) for the Adder and QAOA benchmarks as shown in Figure 12. TUSQ consistently performs at least $10\times$ better than TQSim. On average (geometric mean) TUSQ performs $68.6\times$ and upto $493.4\times$ faster than TQSim.

VII. CONCLUSION

We propose TUSQ, a simulator for efficient noisy simulation of quantum circuits. In order to keep the memory footprint low, noisy simulation of a quantum circuit is performed by

sampling stochastic noisy channels, and averaging the output of multiple quantum circuits with fixed noisy gates sampled from the channels. This increase in the number of quantum circuits leads to significantly longer times for noisy simulation compared to noiseless simulation. To reduce this increased circuit overhead, and subsequently reduce simulation time, TUSQ consists of two components - the *Error Characterization Module* (ECM), and the *Tree-based Execution Module* (TEM). The ECM uses a low cost intermediate representation called *Error Realization* (ER) to find circuits which produce the same output and performs a single simulation for all of them. After the ECM obtains a minimal set of distinct circuits, the TEM reuses computation across these circuits. This computational reuse is facilitated by representing these circuits together as a tree. The TEM samples the significant leaf nodes of this tree and prunes the remaining ones. It traverses this tree using depth-first search and uses uncomputation to perform rollback-recovery at several stages which reduces simulation time.

We evaluate TUSQ for a total of 186 benchmarks and report an average speedup of $52.5\times$ and $12.53\times$ over Qiskit and CUDA-Q, which goes up to $7878.03\times$ and $439.38\times$ respectively. For larger benchmarks (more than 15 qubits), the average speedup is $55.42\times$ and $23.03\times$ over Qiskit and CUDA-Q respectively. We also evaluate TUSQ against the recently proposed work TQSim [42] for 42 benchmarks, and obtain an average speedup of $68.6\times$ which goes up to $493.4\times$

VIII. ACKNOWLEDGEMENT

This work is funded in part by the STAQ project under award NSF Phy-232580; in part by the US Department of Energy Office of Advanced Scientific Computing Research, Accelerated Research for Quantum Computing Program; and in part by the NSF Quantum Leap Challenge Institute for Hybrid Quantum Architectures and Networks (NSF Award 2016136), in part by the NSF National Virtual Quantum Laboratory program, in part based upon work supported by the U.S. Department of Energy, Office of Science, National Quantum Information Science Research Centers, and in part by the Army Research Office under Grant Number W911NF-23-1-0077. This research used resources of the National Energy Research Scientific Computing Center, a DOE Office of Science User Facility using NERSC award NERSC DDR-ERCAP0032212. The views and conclusions contained in this document are those of the authors and should not be interpreted as representing the official policies, either expressed or implied, of the U.S. Government. The U.S. Government is authorized to reproduce and distribute reprints for Government purposes notwithstanding any copyright notation herein. FTC is the Chief Scientist for Quantum Software at Infleqion and an advisor to Quantum Circuits, Inc. We acknowledge the use of NVIDIA Quantum Cloud resources for preliminary experiments conducted in this research. We also thank Meng Wang for sharing TQSim’s GPU compatible code using which we executed some benchmarking experiments.

REFERENCES

- [1] “Hamming weight,” https://en.wikipedia.org/wiki/Hamming_weight, accessed: 2025-03-27.
- [2] “Ibm quantum experience,” <https://quantum-computing.ibm.com>, accessed: 2025-4-9.
- [3] “Qiskit statevector simulator - gpu,” https://qiskit.github.io/qiskit-aer/stubs/qiskit_aer.StatevectorSimulator.html.
- [4] “Quantinuum cloud access,” <https://www.quantinuum.com/products-solutions/quantinuum-systems>, accessed: 2025-4-9.
- [5] “Quera cloud access,” <https://www.quera.com/premium-access>.
- [6] H. Bayraktar, A. Charara, D. Clark, S. Cohen, T. Costa, Y.-L. L. Fang, Y. Gao, J. Guan, J. Gunnels, A. Haidar *et al.*, “cuquantum sdk: A high-performance library for accelerating quantum science,” in *2023 IEEE International Conference on Quantum Computing and Engineering (QCE)*, vol. 1. IEEE, 2023, pp. 1050–1061.
- [7] Y.-T. Chen, C. Farquhar, and R. M. Parrish, “Low-rank density-matrix evolution for noisy quantum circuits,” *npj Quantum Information*, vol. 7, no. 1, p. 61, 2021.
- [8] S. A. Cuccaro, T. G. Draper, S. A. Kutin, and D. P. Moulton, “A new quantum ripple-carry addition circuit,” *arXiv preprint quant-ph/0410184*, 2004.
- [9] J. Dalibard, Y. Castin, and K. Mølmer, “Wave-function approach to dissipative processes in quantum optics,” *Physical review letters*, vol. 68, no. 5, p. 580, 1992.
- [10] P. Das, C. A. Pattison, S. Manne, D. M. Carmean, K. M. Svore, M. Qureshi, and N. Delfosse, “Afs: Accurate, fast, and scalable error-decoding for fault-tolerant quantum computers,” in *2022 IEEE International Symposium on High-Performance Computer Architecture (HPCA)*. IEEE, 2022, pp. 259–273.
- [11] E. Farhi, J. Goldstone, and S. Gutmann, “A Quantum Approximate Optimization Algorithm,” Nov. 2014.
- [12] D. García-Martín, M. Larocca, and M. Cerezo, “Effects of noise on the overparametrization of quantum neural networks,” *Physical Review Research*, vol. 6, no. 1, p. 013295, 2024.
- [13] J. Ghosh, A. G. Fowler, and M. R. Geller, “Surface code with decoherence: An analysis of three superconducting architectures,” *Physical Review A—Atomic, Molecular, and Optical Physics*, vol. 86, no. 6, p. 062318, 2012.
- [14] C. Gidney, “Stim: a fast stabilizer circuit simulator,” *Quantum*, vol. 5, p. 497, Jul. 2021. [Online]. Available: <https://doi.org/10.22331/q-2021-07-06-497>
- [15] J. Gince, “Fermionic machine learning,” 2023. [Online]. Available: <https://github.com/MatchCake/MatchCake>
- [16] J. Gince, J.-M. Pagé, M. Armenta, A. Sarkar, and S. Kourtis, “Fermionic machine learning,” 2024.
- [17] L. K. Grover, “A fast quantum mechanical algorithm for database search,” in *Proceedings of the twenty-eighth annual ACM symposium on Theory of computing*, 1996, pp. 212–219.
- [18] A. Holmes, M. R. Jorak, G. Pasandi, Y. Ding, M. Pedram, and F. T. Chong, “Nisq+: Boosting quantum computing power by approximating quantum error correction,” in *2020 ACM/IEEE 47th annual international symposium on computer architecture (ISCA)*. IEEE, 2020, pp. 556–569.
- [19] Y. Huang, S. Holtzen, T. Millstein, G. Van den Broeck, and M. Martonosi, “Logical abstractions for noisy variational quantum algorithm simulation,” in *Proceedings of the 26th ACM international conference on architectural support for programming languages and operating systems*, 2021, pp. 456–472.
- [20] S. Jiang, Y.-H. Chung, C.-C. Chang, T.-Y. Ho, and T.-W. Huang, “Bqsim: Gpu-accelerated batch quantum circuit simulation using decision diagram,” in *Proceedings of the 30th ACM International Conference on Architectural Support for Programming Languages and Operating Systems, Volume 2*, 2025, pp. 79–94.
- [21] S. Jiang, R. Fu, L. Burgholzer, R. Wille, T.-Y. Ho, and T.-W. Huang, “Flatdd: A high-performance quantum circuit simulator using decision diagram and flat array,” in *Proceedings of the 53rd International Conference on Parallel Processing*, 2024, pp. 388–399.
- [22] T. Jones, A. Brown, I. Bush, and S. C. Benjamin, “Quest and high performance simulation of quantum computers,” *Scientific reports*, vol. 9, no. 1, p. 10736, 2019.
- [23] A. Kandala, A. Mezzacapo, K. Temme, M. Takita, M. Brink, J. M. Chow, and J. M. Gambetta, “Hardware-efficient variational quantum eigensolver for small molecules and quantum magnets,” *Nature*, vol. 549, no. 7671, pp. 242–246, 2017.

- [24] R. Koo and S. Toueg, "Checkpointing and rollback-recovery for distributed systems," *IEEE Transactions on Software Engineering*, no. 1, pp. 23–31, 1987.
- [25] A. Li, B. Fang, C. Granade, G. Prawiroatmodjo, B. Heim, M. Roetteler, and S. Krishnamoorthy, "Sv-sim: scalable pgas-based state vector simulation of quantum circuits," in *Proceedings of the International Conference for High Performance Computing, Networking, Storage and Analysis*, 2021, pp. 1–14.
- [26] A. Li, O. Subasi, X. Yang, and S. Krishnamoorthy, "Density matrix quantum circuit simulation via the bsp machine on modern gpu clusters," in *Sc20: international conference for high performance computing, networking, storage and analysis*. IEEE, 2020, pp. 1–15.
- [27] G. Li, Y. Ding, and Y. Xie, "Eliminating redundant computation in noisy quantum computing simulation," in *2020 57th ACM/IEEE Design Automation Conference (DAC)*. IEEE, 2020, pp. 1–6.
- [28] Y. Li and S. C. Benjamin, "Efficient variational quantum simulator incorporating active error minimization," *Phys. Rev. X*, vol. 7, p. 021050, Jun 2017. [Online]. Available: <https://link.aps.org/doi/10.1103/PhysRevX.7.021050>
- [29] S. F. Lin, J. Viszlai, K. N. Smith, G. S. Ravi, C. Yuan, F. T. Chong, and B. J. Brown, "Codesign of quantum error-correcting codes and modular chiplets in the presence of defects," in *Proceedings of the 29th ACM International Conference on Architectural Support for Programming Languages and Operating Systems, Volume 2*, 2024, pp. 216–231.
- [30] D. Lykov, R. Shaydulin, Y. Sun, Y. Alexeev, and M. Pistoia, "Fast simulation of high-depth qaoa circuits," in *Proceedings of the SC'23 Workshops of The International Conference on High Performance Computing, Network, Storage, and Analysis*, 2023, pp. 1443–1451.
- [31] K. Mølmer and Y. Castin, "Monte carlo wavefunctions in quantum optics," *Quantum and Semiclassical Optics: Journal of the European Optical Society Part B*, vol. 8, no. 1, p. 49, 1996.
- [32] M. A. Nielsen and I. L. Chuang, "Quantum computation and quantum information," *Phys. Today*, vol. 54, no. 2, p. 60, 2001.
- [33] T. L. Patti, T. Nguyen, J. G. Lietz, A. J. McCaskey, and B. Khailany, "Augmenting simulated noisy quantum data collection by orders of magnitude using pre-trajectory sampling with batched execution," *arXiv preprint arXiv:2504.16297*, 2025.
- [34] A. Peruzzo, J. McClean, P. Shadbolt, M.-H. Yung, X.-Q. Zhou, P. J. Love, A. Aspuru-Guzik, and J. L. O'Brien, "A variational eigenvalue solver on a photonic quantum processor," *Nature communications*, vol. 5, no. 1, p. 4213, 2014.
- [35] M. B. Plenio and P. L. Knight, "The quantum-jump approach to dissipative dynamics in quantum optics," *Reviews of Modern Physics*, vol. 70, no. 1, p. 101, 1998.
- [36] G. S. Ravi, K. N. Smith, P. Gokhale, and F. T. Chong, "Quantum computing in the cloud: Analyzing job and machine characteristics," in *2021 IEEE International Symposium on Workload Characterization (IISWC)*. IEEE, 2021, pp. 39–50.
- [37] P. W. Shor, "Polynomial-time algorithms for prime factorization and discrete logarithms on a quantum computer," *SIAM Journal on Computing*, vol. 26, no. 5, p. 1484–1509, Oct 1997. [Online]. Available: <http://dx.doi.org/10.1137/S0097539795293172>
- [38] M. Smelyanskiy, N. P. Sawaya, and A. Aspuru-Guzik, "qhipster: The quantum high performance software testing environment," *arXiv preprint arXiv:1601.07195*, 2016.
- [39] T. Tomesh, P. Gokhale, V. Omole, G. S. Ravi, K. N. Smith, J. Viszlai, X.-C. Wu, N. Hardavellas, M. R. Martonosi, and F. T. Chong, "Supermarq: A scalable quantum benchmark suite," in *IEEE International Symposium on High-Performance Computer Architecture (HPCA)*, 2022.
- [40] M. Wang, F. Hua, C. Liu, N. Bauman, K. Kowalski, D. Claudino, T. Humble, P. Nair, and A. Li, "Enabling scalable vqe simulation on leading hpc systems," in *Proceedings of the SC'23 Workshops of The International Conference on High Performance Computing, Network, Storage, and Analysis*, 2023, pp. 1460–1467.
- [41] M. Wang, R. Huang, S. Tannu, and P. Nair, "Tqsim: a case for reuse-focused tree-based quantum circuit simulation," *arXiv preprint arXiv:2203.13892*, 2022.
- [42] M. Wang, S. Tannu, and P. J. Nair, "Accelerating simulation of quantum circuits under noise via computational reuse," in *Proceedings of the 52nd Annual International Symposium on Computer Architecture*, 2025, pp. 1539–1553.
- [43] S. Wang, E. Fontana, M. Cerezo, K. Sharma, A. Sone, L. Cincio, and P. J. Coles, "Noise-induced barren plateaus in variational quantum algorithms," *Nature communications*, vol. 12, no. 1, p. 6961, 2021.
- [44] C. J. Wood, "Special session: Noise characterization and error mitigation in near-term quantum computers," in *2020 IEEE 38th International Conference on Computer Design (ICCD)*. IEEE, 2020, pp. 13–16.
- [45] X.-C. Wu, S. Di, E. M. Dasgupta, F. Cappello, H. Finkel, Y. Alexeev, and F. T. Chong, "Full-state quantum circuit simulation by using data compression," in *Proceedings of the International Conference for High Performance Computing, Networking, Storage and Analysis*, 2019, pp. 1–24.
- [46] C. Zhang, Z. Song, H. Wang, K. Rong, and J. Zhai, "Hyquas: hybrid partitioner based quantum circuit simulation system on gpu," in *Proceedings of the 35th ACM International Conference on Supercomputing*, 2021, pp. 443–454.
- [47] Y. Zhao, Y. Guo, Y. Yao, A. Dumi, D. M. Mulvey, S. Upadhyay, Y. Zhang, K. D. Jordan, J. Yang, and X. Tang, "Q-gpu: A recipe of optimizations for quantum circuit simulation using gpus," in *2022 IEEE International Symposium on High-Performance Computer Architecture (HPCA)*. IEEE, 2022, pp. 726–740.
- [48] A. Zulehner and R. Wille, "Advanced simulation of quantum computations," *IEEE Transactions on Computer-Aided Design of Integrated Circuits and Systems*, vol. 38, no. 5, pp. 848–859, 2018.